Nanoscale

Accepted Manuscript

ROYAL SOCIETY
OF CHEMISTRY

www.rsc.org/nanoscale

ARTICLE

Liquid-Solid Spinodal Decomposition Mediated Synthesis of Sb$_2$Se$_3$ Nanowires and Their Photoelectric Behavior

Yong Hun Kwon[a], Myoungho Jeong[b,c], Hyun Woo Do[a], Jeong Yong Lee[b,c], and Hyung Koun Cho*[a]

The convenient synthesis of one-dimensional nanostructures of chalcogenide compounds with a visible band-gap is an essential research topic in developing the next-generation photoelectronic devices. In particular, the design of a theoretically predictable synthesis process provides great flexibility and has a considerable ripple effect throughout nanotechnology. In this study, a novel rational growth approach is designed using the spinodal decomposition phenomenon for the synthesis of the Sb$_2$Se$_3$ nanowires, which is based on the thermodynamic phase diagram. Using a stacked elemental layer (Sb/Sb-Se/Se) and heat treatment at 623 K for 30 min in N$_2$ atmosphere, the vertically inclined one-dimensional nanostructures are experimentally demonstrated. An additional annealing process at 523 K in vacuum effectively removed excess Se elements due to their high vapor pressure, resulting in highly dense single crystal Sb$_2$Se$_3$ nanowire arrays. Adapting our synthesis approach enables significantly improved photocurrent generation in the vertically stacked structure (glass/ITO/Sb$_2$Se$_3$ nanowires/ITO/PEN) from 6.4 (dark) to under 690 μA (at 3 V under AM 1.5 G). In addition, a photoelectrochemical test demonstrated the *p*-type conductivity and the robust photocorrosion performance in 0.5 M H$_2$SO$_4$.

Introduction

Inorganic semiconducting materials having one-dimensional (1D) nanostructures (nanowires, nanotubes, nanobelts, and nanorods) have been extensively explored for various electronic and optoelectronic applications due to their interesting properties arising from small dimensions which distinctly differ from bulk nanostructures[1-5]. Their extremely low dimensional shape offers flexibility to control the density of states in semiconductor, optical, and electronic properties, as well as quantum confinement effect, high aspect ratio, and single crystalline structures. Thus, 1D semiconducting nanostructures are widely considered as building blocks for the next generation electronics, photonics, sensors, and energy applications[1-6].

Vapor-liquid-solid (VLS) and vapor-solid are representative mechanisms for the growth of one-dimensional semiconductors, such as nanowires and nanorods, from chemical vapor deposition[1-4]. For the liquid phase assisted VLS method, the growth of nanowires is conveniently predicted using a phase diagram between the semiconductor and metal, and many groups reported that the growth of Si and Ge nanowires agreed well with the prediction from the phase diagram[4, 5]. The creation of Au-Si alloy droplets induced by thermal annealing at temperatures higher than the Au-Si eutectic point induces 1D crystalline nanowires grown by a liquid metal-Si alloy droplet. As a result, the Si with much higher melting point than liquid metal alloys precipitates at the liquid-alloy/Si interface. This process requires the assistance of a liquid phase for the supersaturation[4, 5]. The discovery of the liquid phase related VLS mechanism seems to have increased the intense research on the synthesis of 1D nanostructures using various semiconductors[1, 3]. Thus, compound semiconductors such as ZnO and GaN also employ the VLS process for the growth of nanostructures because of its simple and efficient method[7, 8]. However, this process inevitably induces the incorporation of metal impurities, resulting in non-radiative recombination[5].

Antimony triselenide (Sb$_2$Se$_3$) compound with an orthorhombic structure has an inherent anisotropic crystal structure along the [001] direction, while this anisotropy in most atomic crystals is small[9, 10]. It can promote the synthesis of 1D nanostructures based on the anisotropic nature of crystal growth without metal impurities, resulting in the [001] preferential growth of Sb$_2$Se$_3$[10, 11]. Anisotropic crystallography has the best characteristics for the abnormal 1D growth of compound semiconductors. In addition, the Sb$_2$Se$_3$ in the Sb-Se binary system is only one stable phase, since minerals in nature are dissimilar to Cu-Se and Sn-Se binary[9, 12, 13]. The

a. School of Advanced Materials Science and Engineering, Sungkyunkwan University, 2066 Seobu-ro, Jangan-gu, Suwon, Gyeonggi-do, 440-746, Republic of Korea
b. Center for Nanomaterials and Chemical Reactions, Institute for Basic Science (IBS), 291 Daehak-ro, Yuseong-gu, Daejeon, 305-701, Republic of Korea
c. Department of Materials Science and Engineering, Korea Advanced Institute of Science and Technology (KAIST), 291 Daehak-ro, Yuseong-gu, Daejeon, 305-701, Republic of Korea

Sb_2Se_3 exhibits a direct band-gap of ~ 1.2 eV and has a layered structure suitable for photoelectric and thermoelectric applications. Nevertheless, few groups have studied the synthesis of 1D Sb_2Se_3 and the research approach is based on the vacuum evaporation method. In particular, D. Wang et al. and Y. Liu et al. reported experimental results on the blue-shift of direct band-gap to 1.46 eV and 1.5 eV appropriate for the photovoltaic cells[14, 15]. Also, the extremely practical 1D photodetecting property of $(Sb_{1-x}Bi_x)_2Se_3$ nanowires was demonstrated with a single nanowire under red light (639 nm)[16]. However, no reports have been presented on the synthesis of large scale and vertical arrayed 1D Sb_2Se_3[10, 14-19].

  In this study, growth mechanism of spinodal decomposition liquid-solid is suggested for the growth of single crystalline Sb_2Se_3 nanowires, where our process design is based on a thermodynamic phase diagram. The electrodeposited Sb/Sb-Se and the evaporated Se (final structure: Sb/Sb-Se/Se) layers were used as precursors and were thermally treated using two-step annealing. The growth evolution of the 1D Sb_2Se_3 nanowires is proposed based on microstructural analysis. Moreover, we investigate photoelectric applications using 1D Sb_2Se_3 nanostructures as photo active materials.

Results and discussion

We simply synthesized the vertically inclined single crystalline binary Sb_2Se_3 nanowires, which is based on an annealing process suitable for a large scale synthesis. Firstly, precursors were prepared using an electrodeposition method with salt-containing electrolyte solutions containing Sb and Se ions. Sufficient potential for the simultaneous deposition of Sb and Se, -1400 mV (vs Ag/AgCl) was continuously applied until the total charge density reached 1 Ccm^{-2}. Metal ions are converted to metals or metallic compounds on the cathode surface. Normally, the deposition of multielement compounds such as binary, ternary, or quaternary compounds is more complex as the different elements have different redox potentials and reduction kinetics. The Sb-Se compounds are Se poor, and the stoichiometric Sb_2Se_3 crystals necessitate an additional Se supply. Thus, secondly, these precursors were thermal-annealed at 623 K for 30 min after the deposition of additional Se layer (~ 5 μm) using a thermal evaporation system. The post-annealing was performed in a Se-rich environment with an additional Se coating, resulting in stoichiometric Sb-Se compounds. Interestingly, after the removing of the Se residue at 523 K in vacuum, our approach revealed that these precursors were effectively transformed to the vertically inclined nanowires having an average diameter of ~ 200 nm and length of ~ 4 μm, as shown in Figure 1(a). Figure 1(b) shows the x-ray diffraction (XRD) spectra for the precursors before the additional Se coating, the sample annealed at 523 K, and the nanowires resulting from thermal annealing. Only Sb related peaks in the electrodeposited precursors were observed, except for indium tin oxide (ITO) diffraction peaks,
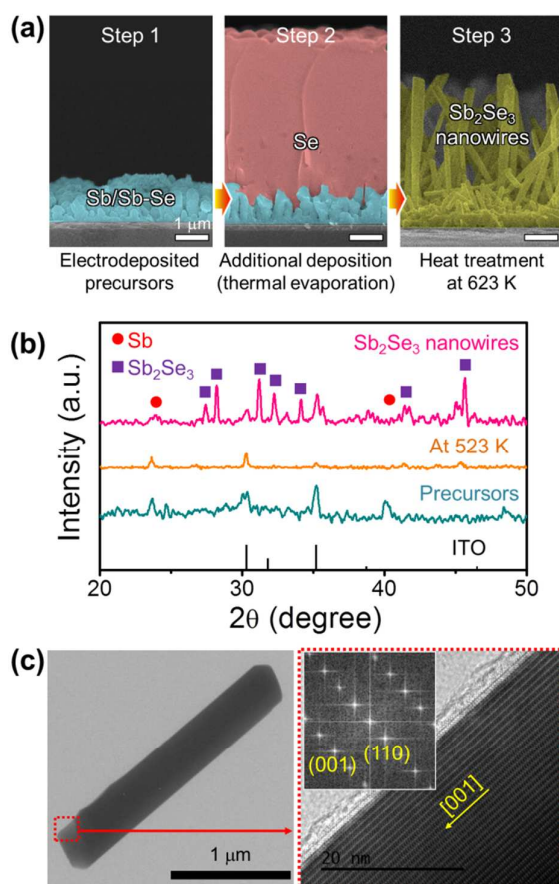
Fig 1. (a) Cross-sectional SEM images of electrodeposited Sb/Sb-Se precursor, after an additional Se coating on Sb/Sb-Se precursor, and the Sb_2Se_3 nanowires synthesized by simple heat treatment. (b) XRD spectra of the Sb/Sb-Se precursor, the sample annealed at 523 K and the Sb_2Se_3 nanowires. (c) TEM image of single crystalline Sb_2Se_3 nanowire and HRTEM image and fast Fourier transform filtered diffraction pattern showing its crystallographic characteristic.

while the Sb-Se compounds and Se peaks were not detected. At 523 K, a weak peak related with the Sb_2Se_3 was detected around 45.3°. After the annealing of the precursors, obtained nanowires showed the distinct Sb_2Se_3 diffraction peaks and faint Sb peaks. This indicates that the precursors were predominantly changed to the 1D structured Sb_2Se_3 crystals. It is also revealed in the detailed microstructures using field-emission transmission electron microscopy (TEM), as shown in Figure 1(c). The high-resolution TEM (HRTEM) image and fast Fourier transform filtered diffraction pattern exhibit the presence of the preferred growth along the (001) plane of Sb_2Se_3 nanostructures with the atomically smooth side facets, and the d-spacing value of 0.39 nm is coincident with the expected value of the Sb_2Se_3 crystals[19].

  In the synthesis of these Sb_2Se_3 nanostructures, the process design can be artificially deduced from the thermodynamic phase diagram[20]. The key consideration for the process design is based on the fact that some compounds have an immiscibility gap between the solid compounds and liquid phase, and this characteristic is expected in PbS, PbSe, PbTe,

SnTe, GeTe, Sb_2Se_3 and so on. Among these, the Sb-Se binary compound has a peculiar thermodynamic property, whereby a stable compound is only in the Sb_2Se_3 phase, unlike Cu-Se compounds with various stoichiometric phases[9, 12]. In particular, the Sb-Se binary compound has a strong potential for photovoltaic applications such as solar cells and photoelectrochemical cells since its band-gap is suitable for the absorption of the visible spectrum[9].

Figure 2(a) shows the calculated Sb-Se phase diagram using the associated solution model[20]. Here, the gray color is the region corresponding to the coexistence of the liquid phase and the solid Sb_2Se_3 compound. This region can be produced when the temperature and Se at% are more than 494 K and 60 at%, respectively. Interestingly, from the thermodynamic phase diagram, the Sb-Se phase in this region is theoretically expected to show spinodal decomposition with the unmixing of liquid and solid, resulting in the phase separation phenomenon between the two coexisting phases. As a more practical approach, spinodal decomposition can provide a meaningful means of producing stable binary compounds embedded in a liquid phase, which can be treated by purely diffusional growth. Ideally, this expectation was adopted to synthesize the Sb_2Se_3 nanostructures in this study, where the nucleated solid compounds start to cluster together throughout the liquid at a liquid-solid coexistence temperature. The key parameters in this crystallization process are the temperature and Sb-Se precursor ratio, based on the thermodynamic phase diagram. First, we simply categorized the composition of the specimens into relatively Sb-rich, intermediate mixed Sb-Se, and nearly pure Se, as indicated by the arrows in Figure 2(a). Also, their phase changes are expected to follow the vertical arrows indicated as routes R_1, R_2, and R_3 during the elevation of the reaction temperature. In the relatively Sb-rich route R_1, no phase transitions are anticipated due to the temperature variation below 700 K and our maximum process temperature is 623 K. In contrast, the R_2 line in the mixed Sb-Se containing Se at more than 60 at% should pass through the miscibility gap corresponding to spinodal decomposition above 494 K. Theoretically, it is expected that the phase separation into the solid stoichiometric Sb_2Se_3 and liquid Se phases with small Sb contents could occur during the annealing process. Finally, the R_3 indicates that pure Se is melted to a liquid phase at 494 K. According to the phase diagram, it is estimated that only the Sb of 0.07 at% can dissolve into the liquid phase due to low solubility limit at this temperature. The solubility of Sb is slightly increased at a higher temperature (nearly 2 at% at 623 K). Consequently, it is anticipated that above 494 K, the Se rich region in the Sb-Se system consists of a solid Sb_2Se_3 phase and liquid Sb doped Se phase. In addition, the immediate nucleation of the Sb_2Se_3 in the mixed Sb-Se can be predicted at around 494 K and the reactants for the Sb_2Se_3 growth can be supplied from the liquid Sb doped Se phase by a diffusion controlled mechanism. Furthermore, the Sb_2Se_3 compound has
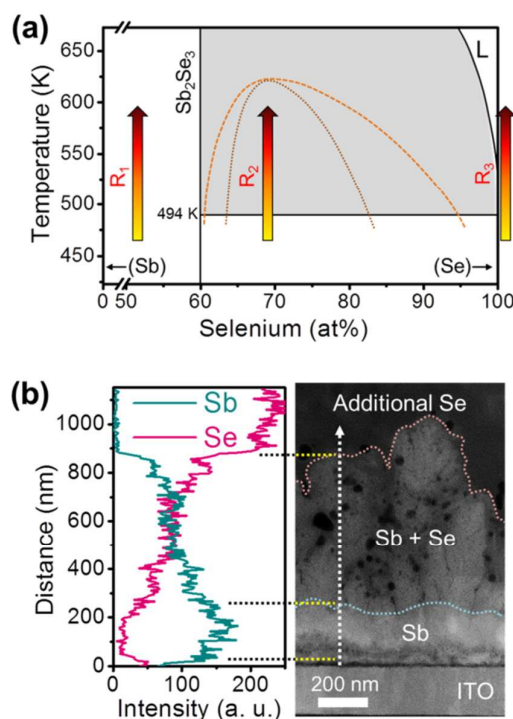
Fig. 2. (a) Calculated Sb-Se binary phase diagram using the associated solution model. R_1, R_2, and R_3 indicate the expected phase transformation during the annealing of the precursors having various compositions. (b) EDS line scan profile for Sb and Se elemental distribution along the vertical direction of the Sb/Sb-Se/Se precursors.

an inherent and highly anisotropic crystal structure along the [001] direction. It can promote the synthesis of 1D nanostructures based on the anisotropic nature of crystal growth without metal impurities, resulting in the [001] preferential growth of Sb_2Se_3.

To verify our design for the synthesis of 1D Sb_2Se_3 nanostructures using phase separation, we prepared a Sb/Sb-Se/Se stacked structure. This structure is appropriate for confirming the reaction of each route simultaneously. For the Sb/Sb-Se structures, electrodeposition was first carried out at various potentials and -1400 mV (vs Ag/AgCl) was optimally determined (Supporting Information, Determining the applied potential). At the potential of -1400 mV, the SbO^+ ions are sufficient near the substrates before the electrodeposition process, and strongly inhibit the reduction of Se (IV) to Se (0). Thus, the Sb metal ions were preferentially deposited and the Se deposition was restricted at the initial stage. As the process progressed, however, these SbO^+ ions were depleted near the surface of the working electrode and the reduction of Se was gradually enhanced. As a result, the Sb and Se could be co-deposited with diffusion controlled reaction, after the initial deposition of the Sb layer, as shown in Figure 2(b). The film morphology showing a dendritic structure with high specific surface area of the mixed Sb-Se layer is indirect evidence of chemical reaction governed by ion diffusive growth mechanism[21, 22]. In addition, the average Sb and Se

composition ratios are estimated to be 73.6 and 26.4 at%, respectively (Supporting Information Figure S1). Therefore, to produce the stoichiometric Sb_2Se_3, enough additional Se layers (~ 5 µm) were deposited on the electrodeposited Sb-Se layer by thermal evaporation, as shown in Figure 1(a). The Se rich atmosphere is appropriate since the remaining Se residue can be easily removed after the heat treatment due to the high vapor pressure[9, 23].

These precursors were then thermal treated for the Sb_2Se_3 synthesis using a two-step rapid thermal annealing (RTA) system at different temperatures. The annealing procedure was performed at 623 K for 30 minutes in an N_2 atmosphere (~ 40 kPa) for the synthesis of Sb_2Se_3 crystals, and an additional thermal treatment was then carried out to completely remove the remaining Se residues at 523 K in a vacuum, as shown in Figure 3(a). As indicated by the circles in Figure 3(a), the thermal treatments were interrupted at 423, 523, and 623 K during the ramping up stage, as shown in Figures 3(d-f), respectively, to investigate the growth evolution of the Sb_2Se_3 crystals. Compared to the sample before the annealing [Figure 3(c)], the small-size protrusions of the crystal phase in the surface morphology are exposed by thermal treatment up to 523 K, since the liquidus line for Se is 494 K in air ambient and the Se on the surface becomes partially vaporized[9, 20]. At 623 K, these protrusions are distinctly observed and their shape also shows clear crystal side facets [Figure 3(f)]. On the other hand, the space among the protrusions seems to be in amorphous phases, considering the smooth surface. Energy dispersive spectroscopy (EDS) and diffraction pattern confirmed that this may be attributed to the rapid cool-down from the melted liquid phase after thermal treatment (Supporting Information Figure S2). Surprisingly, these amorphous phases are completely removed by the second annealing step (at 523 K in vacuum), and as a result, Sb_2Se_3 nanowires with high density are produced, as shown in Figures 1(b-c), and 3g. Furthermore, the nanowires with rectangular shape are synthesized with the vertically inclined alignment, which is profitable in manufacturing the nanostructured devices at a wafer scale. Successful synthesis of the 1D nanostructure demonstrates the agreement between the experimental results and the prediction from the phase diagram.

To determine the procedure of the chemical reaction during the thermal annealing of the precursors, the mapping for the elemental distribution of the Sb and Se was carried out using an areal scan of the EDS for the samples annealed at different temperatures (423, 523, and 623 K), as shown in Figures 4(a-c). Due to the overlapping of the Sb Lα (3.604 keV) and Sn Lα (3.444 keV) x-ray spectra, the Sn in the ITO layer also appears in the detection of the Sb element[24]. From the cross-sectional images, the Sb/Sb-Se/Se stacked structure is not significantly changed at 423 K, since the annealing temperature is not high enough for the transformation. When the annealing temperature reached 523 K, the dendritic Sb-Se layer was transformed to stoichiometric Sb_2Se_3 crystalline, which can be confirmed by the brighter Se contrast shown in Figure 4(b) than that in Figure 4(a). In addition, the top region consisted of the amorphous Se produced from the liquid phase due to the low-melting temperature of pure Se, 494 K (Supporting Information Figure S2). However, the initial Sb layer (~ 250 nm) at the bottom region maintains a nearly pure Sb phase even at 523 K, considering there is no significant contrast change in this region. This indicates the suppression of the diffusion of Se atoms to the Sb-layer. In contrast, the thermal annealing at 623 K makes the initial Sb layer disappear and the length of the Sb_2Se_3 nanostructures is abruptly increased, as shown in Figure 4(c). It seems that the Sb at the bottom region supplies cation metal precursors for the reaction with liquid Se under a sufficient thermal temperature, resulting in the longer nanostructure of Sb_2Se_3 compounds. Interestingly, amorphous Se (liquid phase at high temperature) with low Sb contents was used not only as a reactant but also as a mediate for the diffusion pathway of dissolved Sb. The Se layer in the top region disappeared completely after thermal annealing at 523 K and under vacuum. Since amorphous Se originated from the rapid cool-down of the liquid phase, vacuum annealing at 523 K in the second step causes the vaporization of the excess Se elements with quite a high vapor pressure and remains only in the solid phase Sb_2Se_3 compounds. Thus, it is considered that the formation of the nanostructure Sb_2Se_3 using liquid-solid
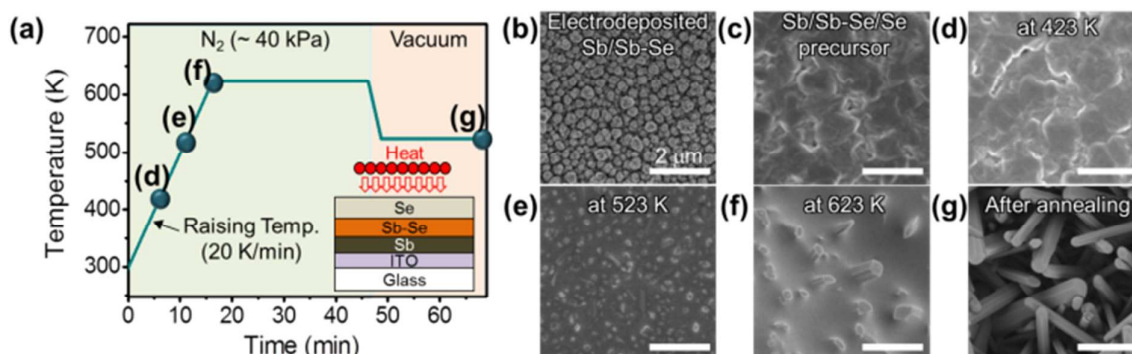
Fig. 3. (a) Process flow for thermal treatment used for the synthesis of Sb_2Se_3 nanowires. Top-view SEM images for (b) as-deposited Sb/Sb-Se precursor, (c) after an additional Se coating on Sb/Sb-Se precursor, samples interrupted at (d) 423, (e) 523, and (f) 623 K during ramping up for thermal treatment, and (g) Sb_2Se_3 nanowires after the evaporation of Se residue at 523 K.

ARTICLE

spinodal decomposition shows that the diffusion controlled growth mechanism prevailed due to the supply of the Sb metal element, due to the presence of a sufficient liquid Se phase. Consequently, when the precursors of the Sb/Sb-Se/Se stacked structure were annealed in RTA, the mixed Sb-Se layers were crystallized to the Sb_2Se_3, where the Sb_2Se_3 phase exhibited preferential growth behavior along the [001] direction due to its natural crystallographic anisotropy [Figure 1(c)]. Finally, the dimension of the Sb_2Se_3 nanostructure was determined by the diffusion of the Sb element from the bottom region or the Sb doped Se region. This growth behavior closely matched the expectation of the theoretical thermodynamic phase diagram. Figure 4(d) shows schematic diagrams to show the formation mechanism of the nanowires. The Sb, mixed Sb-Se, and additional Se layers followed the routes of R_1, R_2, and R_3, respectively, during the post-annealing as introduced in Figure 2(a). In the region of route R_1, no abrupt change in Sb was experimentally observed during the temperature elevation from 423 to 523 K. The mixed Sb-Se layer (route R_2) was decomposed into solid Sb_2Se_3 and liquid Sb-doped Se due to the spinodal mechanism, and the Sb-Se layer of dendritic structure with a high density surface area was preferentially crystallized. The liquid Se in route R_3 was observed at 523 K in our experiment, due to its low melting point (~ 494 K). At 623 K, the effective Sb diffusion occurred from the initial Sb layer into the Sb_2Se_3 crystal [Figure 4(c)].

The synthesis of nanowires via electrodeposition and heat treatment was attempted for Zn-Sb and γ-Bi_2MoO_6[25, 26]. Previously, electrodeposited precursors having agglomerated particles were used. In these experiments, diffusion and chemical reaction occurred within the agglomerated area and only randomly oriented structures were possible. In addition, the remaining residue of the excess elements restricted the manufacturing of the devices. Thus, additional treatment to

selectively eliminate these residues should be developed. However, we successfully synthesized the vertically inclined Sb_2Se_3 nanostructures for the first time. Also, our approach may be applied in the Se and S based chalcogenide compounds, since the excess Se and S can be removed due to the relatively higher vapor pressure[27-29].

The optical characteristics of the Sb_2Se_3 nanowire arrays were analyzed, as shown in Figures 5(a-d). The band-gap of the Sb_2Se_3 nanowire was estimated from the plot of $(\alpha h v)^2$ versus hv modified from the transmittance results. Typically, it is known that the bulk Sb_2Se_3 has a direct band-gap of 1.2 eV, and the Sb_2Se_3 synthesized in our experiment exhibits a relatively wide 1.46 eV, which is appropriate as an absorber layer in solar cells (optimum band-gap, 1.5 eV)[14, 15, 30]. The 1D Sb_2Se_3 nanostructures synthesized using hydrothermal and solvothermal methods in the previous studies have been randomly dispersed on the substrates, and thus they required complex alignment and fabrication processes for the formation of an electrode at both ends of the nanowires. On the other hand, the vertical array of the 1D Sb_2Se_3 nanostructures can provide selective growth using the definition of the bottom electrode and vertically stacked photoelectric devices, as shown in Figure 5(a). The flexible polyethylene-naphthalate (PEN) substrates coated with ITO were electrically connected to the top of the Sb_2Se_3 nanowires, and the I-V characteristics were analyzed to investigate the photoresponse under the irradiation of air mass AM 1.5 G (100 mWcm^{-2}). The open area for irradiation was 1 cm^2. Under a dark status, the ITO/Sb_2Se_3/ITO device shows a low current level due to the high electrical resistivity of the Sb_2Se_3 nanowires and the rectifying contact at the Sb_2Se_3/ITO interface (Supporting Information Figure S3). However, it is noticeable that the current flow is substantially increased from 6.4 to 690 μA at 3.0 V under the illumination. Furthermore, reproducible
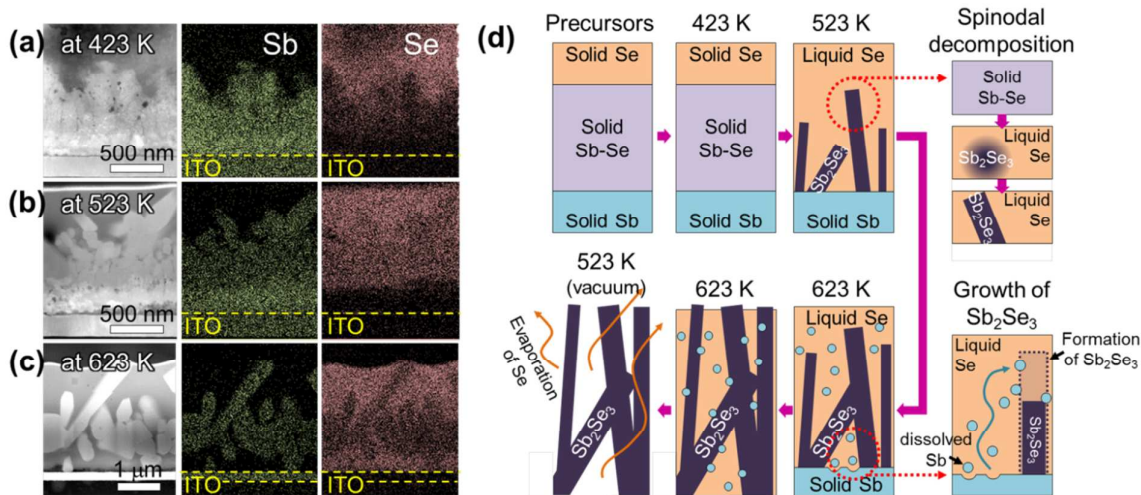
Fig. 4. EDS mapping for Sb L_α (3.604 keV) and Se L_α (3.444 keV) elements after the interruption at (a) 423, (b) 523, and (c) 623 K. (d) Schematic diagram showing detail growth evolution of the Sb_2Se_3 nanowires at each step.

repetition and stable response (on/off ratio = ~ 100) is shown with a rectangular on/off signal, as shown in Figure 5(b). This result reveals that the Sb_2Se_3 compound with a visible bandgap is a good absorber material and effectively generates the photo-carriers. Alternatively, we employed a solid/liquid junction structure, in which the whole surface of the Sb_2Se_3 nanostructure was fully covered with ionic electrolytes for the PEC application. In the PEC system for water splitting, micro- and nanostructures are very promising due to the large surface area used for chemical reaction and charge generation[31]. First, we confirmed the *p*-type characteristic of the synthesized Sb_2Se_3 compound in 0.5 M H_2SO_4, as shown in Figure 5(c). In addition, the Sb_2Se_3 nanostructure array shows a remarkably enhanced photocurrent up to -1.1 mAcm^{-2} from the -0.07 mAcm^{-2} at -300 mV (vs RHE), which is much higher than that of Sb_2Se_3 thin films reported by Y. Lai et al[32]. Consequently, these electrical performances ensure the potential ability of the 1D Sb_2Se_3 nanostructures as absorbers for photoelectric devices. Until now, the most attractive *p*-type photocathode material has been Cu_2O, with a bandgap of 2.1 eV; however, it has corrosive characteristics under ionic solution, showing a rapid reduction process. In practice, the Cu_2O is less stable in the solution having lower pH, while more photocurrent can be obtained. Thus, the use of the passivation layer or thin TiO_2 layer is needed[33, 34]. However, the thermodynamic reduction potential of the Sb_2Se_3 is estimated to be -0.3 V from Gibbs free energy and it anticipates the improved stability of chalcogenide photocathode (Supporting Information, Estimation for the thermodynamic reduction potential of the Sb_2Se_3)[35]. It is sure that current decay was observed within a minute, but the Sb_2Se_3 continuously worked even at 0.5 M H_2SO_4. Moreover, under illumination, the current density of around -40 µAcm^{-2} flowed stably through the device after 120 min. This result indicates that the Sb_2Se_3 is relatively free from the photo-corrosive effects. To apply on the water splitting cells, device structure should be modified and photocatalysts are required for more photocurrent.

Experimental

Preparation of precursors

Aqueous solution containing 0.055 M $K(SbO)C_4H_4O_6\cdot0.5H_2O$ (antimony potassium tartrate), 0.045M H_2SeO_3 (selenous acid), and 1 M NH_4Cl (ammonium chloride) was used as the electrolyte for the Sb_2Se_3 synthesis. The pH of the solution used in the synthesis was approximately 1.8. Ag/AgCl and Pt foil were used as reference and counter electrodes, respectively, in a conventional three electrode system. The glass substrates coated with the 200 nm thick ITO layer were used as working electrodes. Before the deposition, the ITO substrates were consecutively cleaned with acetone, ethanol, and deionized water for 10 min each in an ultrasonic bath. Electrodeposition was potentiostatically carried out at -1400
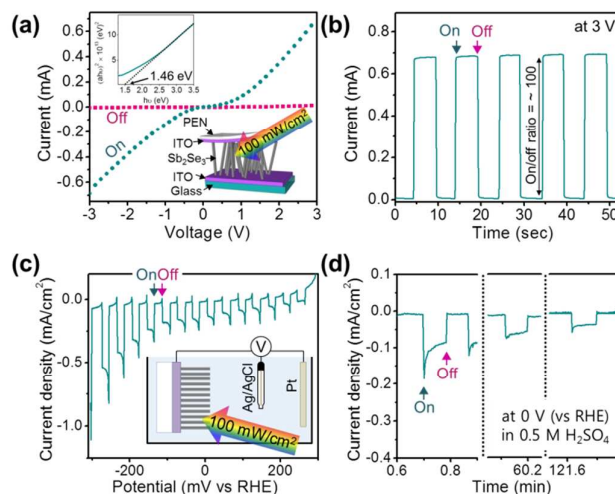
Fig. 5. (a) Current-voltage characteristics of electrically connected Sb_2Se_3 nanowires with/without illumination (the band-gap of Sb_2Se_3 nanowires was estimated from the plot of $(ahv)^2$ versus *hv*, as noticed inset) and (b) illumination on/off characteristics at 3 V. (c) PEC performance and (d) PEC photo-stability result for the Sb_2Se_3 nanowire arrays under the irradiation of AM 1.5 G (100 mWcm^{-2}).

mV and the potential was continuously applied on the substrates until the total charges reached 1 Ccm^{-2}. As a result, the Sb/Sb-Se stacked structure was obtained as a precursor, prior to the thermal treatment. An additional thick Se layer (~ 5 µm) was deposited using a thermal evaporation system to provide enough Se elements during the thermal annealing.

Synthesis of Sb_2Se_3 nanowires

A RTA system was used to produce the designed Sb_2Se_3 nanostructures from the Sb/Sb-Se/Se precursors. To suppress the massive loss of Se with a high vapor pressure, the surface of the samples was covered with corning glass during the thermal treatment. An annealing process was performed at 623 K in N_2 atmosphere (~ 40 kPa) for 30 min. The temperature was increased with the rate of 20 Kmin^{-1}, and after synthesis, additional annealing was continuously carried out at 523 K in a vacuum for the removal of excess Se elements.

Characterization

After the electrodeposition, the structural and compositional characteristics were confirmed by XRD (Bruker AXS D8 Discovery) and EDS (Oxford Instruments, X-Max), respectively, using a field-emission scanning electron microscope (FE-SEM, JEOL, JSM-6700F). The distribution of elements in the Sb/Sb-Se/Se stacked structure was profiled by an EDS line scan depending on annealing temperature. The change in surface morphology during the annealing was also confirmed by SEM and the single crystalline Sb_2Se_3 nanowires were characterized using a TEM (JEOL JEM-2100F).

ARTICLE

Conclusions

In conclusion, we suggested a novel growth mechanism for chalcogenide nanowires based on an expected and convenient synthesis procedure. In the Sb-Se system, the Sb_2Se_3 was the only stable compound and the phase separation into the Sb_2Se_3 solid and Se liquid was expected due to spinodal decomposition. Through the design of the thermal annealing process using this background, we first demonstrated the synthesis of the single crystal Sb_2Se_3 nanowires vertically inclined from the wafer. In this experiment, the Sb/Sb-Se/Se precursors were prepared by electrodeposition and thermal evaporation on the ITO/glass substrates. From the EDS analysis at various temperatures of 423, 523, and 623 K, it was clearly confirmed that the mixed Sb-Se was first crystallized in the Sb_2Se_3 phase embedded in liquid Se by spinodal decomposition. The Sb_2Se_3 growth was controlled by Sb supply which was diffused from the bottom Sb layer and Sb doped liquid Se. As a result, the anisotropic Sb_2Se_3 with orthorhombic structure was grown along the [001] direction. Finally, the remaining Se was evaporated at 523 K and under vacuum due to the differences in vapor pressure between Sb_2Se_3 and Se. A band-gap estimated from the transmittance spectra was 1.46 eV, which is adequate for the photoelectronic application. Interestingly, the extraordinary increase of current ($I_{illumination}/I_{dark}$ = ~ 100) was observed in the vertically stacked structure of the ITO/Sb_2Se_3/ITO under irradiation of AM 1.5G. In addition, the PEC test showed that the photo-stability of the Sb_2Se_3 nanowires in the electrolyte having extremely low pH was considerably better than that of usual p-type Cu_2O photocathode. In principle, our novel growth model for the synthesis of the Sb_2Se_3 nanowires should be applicable to other chalcogenide compounds with a theoretically single binary phase and spinodal decomposition. Furthermore, this synthesis approach is compatible with a wafer based process for a large scale synthesis and vertical alignment from the wafer.

Acknowledgements

Notes and references

1. T. J. Kempa, R. W. Day, S.-K. Kim, H.-G. Park and C. M. Lieber, *Energ. Environ. Sci.*, 2013, **6,** 719.
2. C. M. Lieber, *MRS Bull.*, 2011, **36,** 1052.
3. N. P. Dasgupta, J. Sun, C. Liu, S. Brittman, S. C. Andrews, J. Lim, H. Gao, R. Yan and P. Yang, *Adv. Mater.*, 2014, **26**, 2137.
4. Y. Xia, P. Yang, Y. Sun, Y. Wu, B. Mayers, B. Gates, Y. Yin, F. Kim and H. Yan, *Adv. Mater.*, 2003, **15**, 353.
5. J. Hu, T. W. Odom and C. M. Lieber, *Accounts Chem. Res.*, 1999, **32**, 435.
6. D. C. Kim, B. O. Jung, Y. H. Kwon and H. K. Cho, *J. Electrochem. Soc.*, 2011, **159**, K10.
7. C.-Y. Chen, G. Zhu, Y. Hu, J.-W. Yu, J. Song, K.-Y. Cheng, L.-H. Peng, L.-J. Chou and Z. L. Wang, *ACS Nano*, 2012, **6**, 5687.
8. Y. Gyu-Chul, W. Chunrui and P. Won Il, *Semicond. Sci. Tech.*, 2005, **20**, S22.
9. Y. Zhou, M. Leng, Z. Xia, J. Zhong, H. Song, X. Liu, B. Yang, J. Zhang, J. Chen, K. Zhou, J. Han, Y. Cheng and J. Tang, *Adv. Energy Mater.*, 2014, **4**, 1301846.
10. J. Ma, Y. Wang, Y. Wang, P. Peng, J. Lian, X. Duan, Z. Liu, X. Liu, Q. Chen and T. Kim, *Cryst. Eng. Comm.*, 2011, **13**, 2369.
11. Y. Min, G. D. Moon, C.-E. Kim, J.-H. Lee, H. Yang, A. Soon and U. Jeong, *J. Mater. Chem. C*, 2014, **2**, 6222.
12. R. Heyding, *Canadian Journal of Chemistry*, 1966, **44**, 1233.
13. Y. Feutelais, M. Majid, B. Legendre and S. Frics, *Journal of phase equilibria*, 1996, **17**, 40.
14. Y.-Q. Liu, M. Zhang, F.-X. Wang and G.-B. Pan, *J. Mater. Chem. C*, 2014, **2**, 240.
15. D. Wang, D. Yu, M. Mo, X. Liu and Y. Qian, *J. Crys. Growth*, 2003, **253**, 445.
16. R. Huang, J. Zhang, F. Wei, L. Shi, T. Kong and G. Cheng, *Adv. Funct. Mater.*, 2014, **24**, 3581.
17. D. Choi, Y. Jang, J. Lee, G. H. Jeong, D. Whang, S. W. Hwang, K.-S. Cho and S.-W. Kim, *Sci. Rep.*, 2014, **4**, 6714.
18. W. Farfán, E. Mosquera, R. Vadapoo, S. Krishnan and C. Marín, *J. Nanosci. Nanotechnol.*, 2010, **10**, 5847.
19. J. Ma, Y. Wang, Y. Wang, Q. Chen, J. Lian and W. Zheng, *J. Phys. Chem. C*, 2009, **113**, 13588.
20. G. Ghosh, *J. Phase Equilib.*, 1993, **14**, 753.
21. E. Ben-Jacob, G. Deutscher, P. Garik, N. D. Goldenfeld and Y. Lareah, *Phys. Rev. Lett.*, 1986, **57**, 1903.
22. F. Liu, C. Huang, Y. Lai, Z. Zhang, J. Li and Y. Liu, *J. Alloy. Compd.*, 2011, **509**, L129.
23. L. S. Brooks, *J. Am. Chem. Soc.*, 1952, **74**, 227.
24. Y. H. Wang, K. Y. Chan, X. Y. Li and S. K. So, *Chemosphere*, 2006, **65**, 1087.
25. P. Liu, X. Guo, H. Huang, Q. Yang, Y. Tong and G. A. Hope, *Adv. Mater.*, 2006, **18**, 1873.
26. F.-L. Zheng, G.-R. Li, X.-L. Yu and Y.-X. Tong, *Electrochem. Solid-State Lett.*, 2009, **12**, K56.
27. R. Sharma, J. Lin and Y. Chang, *Metall. Trans. B*, 1987, **18**, 237.
28. J. Lin, R. Sharma and Y. Chang, *J. Phase Equilib.*, 1996, **17**, 253.
29. R. Sharma and Y. Chang, *Bull. Alloy Phase Diagr.*, 1986, **7**, 72.
30. J. J. Loferski, *J. Appl. Phys.*, 1956, **27**, 777.
31. F. E. Osterloh, *Chem. Soc. Rev.*, 2013, **42**, 2294.
32. Y. Lai, Z. Chen, C. Han, L. Jiang, F. Liu, J. Li and Y. Liu, *Appl. Surf. Sci.*, 2012, **261**, 510.
33. A. Paracchino, V. Laporte, K. Sivula, M. Grätzel and E. Thimsen, *Nat. Mater.*, 2011, **10**, 456.
34. C. G. Morales-Guio, S. D. Tilley, H. Vrubel, M. Gratzel and X. Hu, *Nat. Commun.*, 2014, **5**, 3059.
35. S. Chen and L.-W. Wang, *Chem. Mater.*, 2012, **24**, 3659.

Nanoscale Accepted Manuscript